Eur. Phys. J. D **15**, 105–111 (2001)

THE EUROPEAN PHYSICAL JOURNAL D

EDP Sciences

Characterization of a miniature Paul-Straubel trap

C. Champenois, M. Knoop[a], M. Herbane, M. Houssin, T. Kaing, M. Vedel, and F. Vedel

Université de Provence, Physique des Interactions Ioniques et Moléculaires[b], Centre de Saint-Jérôme, Case C21, 13397 Marseille Cedex 20, France

Received 14 November 2000 and Received in final form 1st February 2001

Abstract. Frequency standard applications and ultra-high resolution spectroscopy of a confined single ion require traps of drastically reduced dimensions (about or below 1 mm). These small dimensions increase the sensitivity of the trapping behavior to imperfections in the trap geometry and to patch potentials. For the aim of the metrological laser interrogation of a single Ca^+ ion, a miniature cylindrical ring trap was built. In order to optimize the laser cooling process and to reach strong binding conditions, the boundaries of the stability diagram and the zones of low confinement as well as the ion motion properties were characterized.

PACS. 32.80.Pj Optical cooling of atoms; trapping – 07.75.+h Mass spectrometers

1 Introduction

In recent years the existing classic hyperbolic Paul traps [1] used for experiments in metrology [2], atomic physics [3] and mass spectrometry [4] are often replaced by miniature devices [5], designed and optimized for specific applications [6–9]. Actually, for small and even non-ideal geometry, the effective potential in the trap center is similar to the one of an ideal Paul trap as long as the ion excursion is very small compared to the trap dimensions [10]. For ease of machining and alignment, a cylindrical geometry is often chosen and has been investigated in [8]. A 1 mm-trap proves to be a versatile device since the trapping of an energetic ion cloud can be achieved, as well as the confinement and immobilisation of a single ion with access to low vibration-motion states. In future mass spectrometry, analysis will be drastically shortened by simultaneous trapping of ion clouds in various small devices, the size of each defining a particular mass range [9]. Storing a single ion in such an environment allows to reach the strong binding condition and the Lamb-Dicke regime. Indeed, small traps require very high rf frequencies to reach the necessary storage parameters and therefore imply larger frequencies of motion [11].

Nevertheless, the miniaturization of the trap electrodes does not only have advantageous attributes. The small size of the ion cage makes the potential sensitive to imperfections and flaws. The difference with a pure quadrupole field causes couplings between the axial or radial component of the motion and the rf trapping potential or between the axial and radial motion components only, which contributes by additional frequencies in the motion spectrum [12]. These anharmonicities are the source of the so-called "black canyons" which can exist in the stability diagram [13]. Finally, patch potentials can build up during ion creation which will perturb the electric field. To minimise stray light, laser beams have to be tightly focussed into the center of the trap and imaging has to be designed very precisely. To benefit from all the positive aspects of using a miniature trap, the device must then be tested and its properties carefully investigated.

The present study comes within the project involving the Ca^+ ion for a frequency standard in the optical domain [14,15]. The proposed clock-transition at 729 nm relates the $4S_{1/2}$ ground state and the metastable $3D_{5/2}$ state with a natural linewidth of about 200 mHz [16,17]. One of the principal advantages of Ca^+ is the potential accessibility of all the involved wavelengths by laser diodes.

The outline of the paper is the following. After describing the experimental setup in Section 2, we present the different methods we have employed to characterize the trap. We report on the measurements of the frequencies of the ion motion using an external excitation in Section 3. The following section gives an improved quantification of the miniature trap, that is the limits of the stability diagram and non-linear couplings. Finally, the possible effects of the radiation pressure on the motional properties of the ions will be quantified in Section 5.

2 Experimental setup

Our trap has been designed for metrologic applications based on the laser interrogation of a single ion. Access to the Lamb-Dicke regime, where the first-order Doppler broadening becomes discrete, requires strong confinement of the ions. This can only be achieved with a high confinement frequency $\Omega/2\pi$, involving a trap size of the order

[a] e-mail: mknoop@up.univ-mrs.fr
[b] UMR 6633 CNRS-UAM1

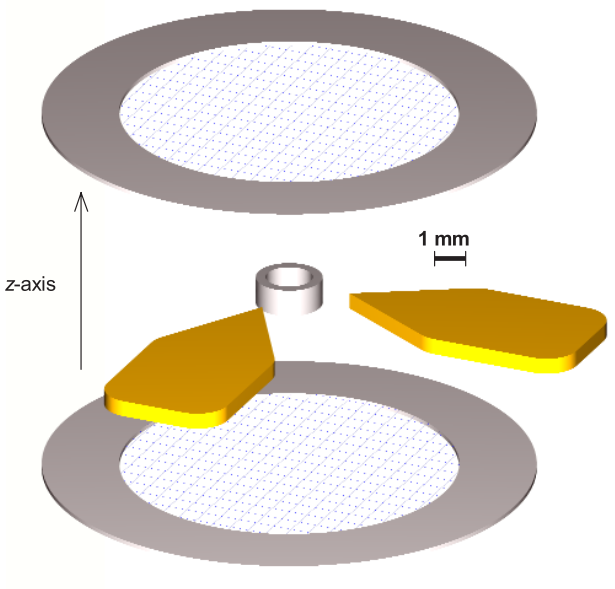

Fig. 1. Artist's view of the cylindrical miniature trap showing the different electrodes for correction of the trap potential.

of a millimeter compatible with the values of the trapping AC voltage experimentally accessible.

For a good visualisation of the confined particles and easy access for the laser beams, a trap geometry of the Paul-Straubel-type [7,8,18] has been chosen. This consists of a cylindrical ring with an inner diameter of $2r_1 = 1.4$ mm and an overall height of $2z_1 = 0.85$ mm (Fig. 1). Two compensation electrodes are formed by flat rings with 13 mm diameter, with their inner openings of 10.5 mm covered by a micrometric wire mesh having a transmission of 86%. These electrodes are placed at a distance of 5.5 mm from the center of the trap and screen the inner volume of the device from electrical stray fields. Application of a constant potential allows then compensation of the resulting trap potential in the z-direction. Small corrections on the confinement potential in the x- and y-direction can be applied by two positioning electrodes tapering into a point in the plane of the ring. In the course of the described experiments all the compensation electrodes were held at ground. Typical working parameters for the rf confinement potential applied to the ring are $\Omega/2\pi = 11.6$ MHz and $V_{\mathrm{AC}} = 700 V_{\mathrm{rms}}$, which leads to a potential well depth of about 9.2 eV. To reduce residual magnetic effects all the electrodes (bulk and mesh) are made from molybdenum with the exception of the two copper positioning electrodes. The complete trap and electrodes assembly is placed in a stainless steel vacuum vessel with an inner diameter of 10 cm. A 100 l/s ion pump can maintain a vacuum pressure below 1×10^{-10} mbar.

Ions are loaded from an atomic calcium beam evaporated from a small oven and ionized inside the trap by electron bombardment. Doppler laser-cooling is carried out on the Ca^+ resonance line $4S_{1/2}$–$4P_{1/2}$ at 397 nm starting at the ion creation. In absence of collisions, synchronous repumping of the low-probability $3D_{3/2}$–$4P_{1/2}$ transition at 866 nm is necessary to maintain an efficient cooling cycle. In the following work, creation parameters have been kept constant to maintain a fixed ion number. A typical cloud contains a few hundreds ions at a temperature of about 300 K. This value is due to the large size of the cloud, and represents an equilibrium between rf heating and laser-cooling.

The laser-cooling of the trapped ions at 397 nm is carried out with a commercial intracavity frequency-doubled titanium-sapphire laser (*Coherent* 899-21). A single-mode laser diode at 866 nm (*SDL* 5402-H1) mounted in a traditional external cavity and stabilized onto a low-finesse ($\mathcal{F} = 200$) reference cavity repumps the ions in the $4P_{1/2}$ level. The two counter-propagating laser beams are reshaped to prepare clean and symmetric waists without astigmatism in the trap center. The diode laser output passes through a singlemode optical fiber. Both beams are tightly focussed into the trap giving waist diameters of less than 60 μm, which cross the trap under an angle of 53 degrees with the z-axis (the observation axis). The laser powers employed in the course of the present experiment are typically about 200 μW for the cooling laser and 500 μW for the repumper.

For the detection of the ions, the fluorescence light at 397 nm is collected by an aspheric lens mounted close to the trap. The optics set-up outside the vessel permits observation of the confined ions using an intensified CCD camera (*Photonic Science* ISIS 4) and a photomultiplier in the photon-counting mode (*Hamamatsu* H-4730). Typical clouds of a couple of hundred ions have a diameter of about 100 μm, which is larger than the waist of the cooling laser. Furthermore, using a sensitive camera makes it possible to see the part of the cloud which corresponds to the fraction of the cooling beam beyond the $1/e^2$ limit which defines the waist.

The experiments devoted to characterizing the quality of ion storage, described below, were performed using two different methods. The first consists in applying an additional AC voltage of small amplitude ("tickle") [19] to one of the endcaps, the other being grounded. If the excitation frequency comes into resonance with one of the ion motion frequencies, the cloud will be heated leading to a decrease of the observed fluorescence signal. Scanning the tickle frequency between 0 to $\Omega/4\pi$ enables us to visualize very precisely all the frequencies of motion, including those resulting from the Mathieu solution as well as the ones induced by possible couplings due to additional nonquadrupolar terms of the real potential. During the second type of investigation, a continuous voltage U_{DC} applied to the connected endcaps was varied adiabatically. This evidences the boundaries of the Mathieu stability diagram and the inhomogeneities due to anharmonicities, as observed previously for standard-sized traps [13,20,21]. This last technique does not imply any external perturbation and measures the storage capability in the absence of any excitation.

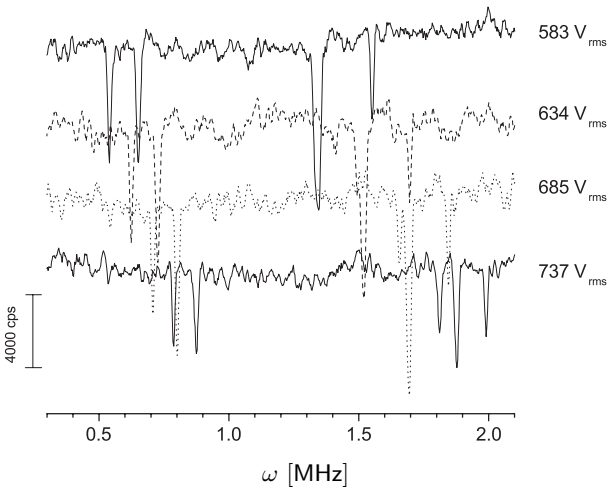

Fig. 2. Fluorescence at 397 nm as function of the applied tickle frequency. The graph shows part of the frequency spectrum of a small Ca^+-ion cloud for different values of V_{AC} and $U_{DC} = 0$. Once the ions are in resonance with the excitation frequency, the energy absorption leads to a sudden decrease of the fluorescence.

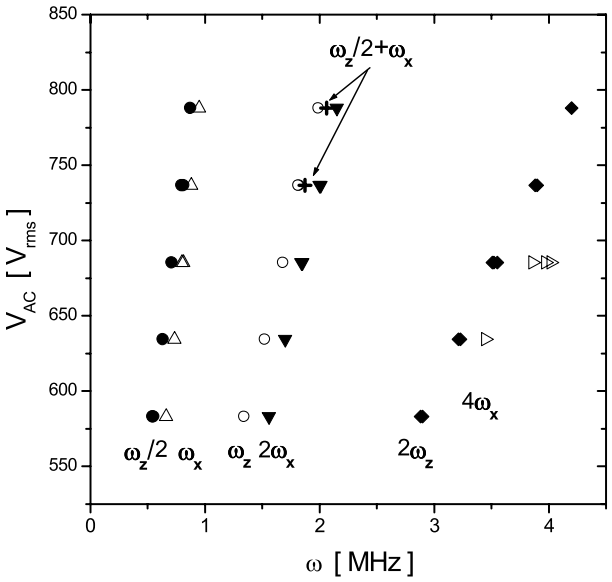

Fig. 3. The various observed frequencies of motion of the ion cloud obtained from frequency spectra as shown in Figure 2. Multiples, submultiples and couplings of the fundamental frequencies are obtained with a precision higher than 99%.

3 Frequencies of motion

The frequency spectrum gives an useful estimate of the dynamic properties of the ion motion and also the efficiency of the confinement in such a device. This has been investigated for different alternative potentials V_{AC} applied to the ring in the case of a constant voltage U_{DC}. The amplitude of the tickle has been chosen to be sufficiently large to reveal the main existing couplings without usually loosing any ions. Figure 2 shows a spectra formed by negative peaks in the variation of the collected fluorescence. The signal loss can reach up to 80% of the overall signal. Indeed, at the occurrence of a mechanical resonance, the energy deposition on the ions in resonance leads to an increase of the Doppler broadening and fewer ions are in resonance with the laser excitation. Moreover, larger trajectories of hotter ions inflate the cloud size and produce a drop in the ion density. Both effects reduce instantaneously the intensity of the fluorescence. While sweeping the tickle frequency, the fluorescence signal after resonance immediately comes back to its initial value, indicating a persistent cooling of the cloud. We can then deduce that the ions do not leave the laser beam during resonance. Occasionally, the breakdown of fluorescence can also be attributed to the effective loss of ions from the trap.

If the confining potential were purely quadrupolar the coefficients of the Mathieu equations could be written as

$$a_z = -2a_x \quad \text{and} \quad q_z = -2q_x \tag{1}$$

with

$$a_z = \frac{8eU_{DC}}{mr_1^2\Omega^2} \quad \text{and} \quad q_z = -\frac{4eV_{AC}}{mr_1^2\Omega^2}\,. \tag{2}$$

The fundamental frequencies $\omega_{x,y,z}/2\pi$ are directly connected to the values of the trapping frequency $\Omega/2\pi$, through the parameters $\beta_{x,y,z}$ [22] by

$$\omega_u = \frac{1}{2}\,\beta_u\Omega \quad \text{with} \quad u = x, y, z. \tag{3}$$

Ideally, $\omega_x = \omega_y$ due to the rotational symmetry of the trap. For $q_z \leq 0.4$, β_u can be calculated with the so-called adiabatic approximation [23]:

$$\beta_u = \sqrt{a_u + \frac{{q_u}^2}{2}}\,. \tag{4}$$

If $U_{DC} = 0$, as it is the case here, $\beta_z = 2\beta_x$ and then ω_z and $2\omega_x$ should be identical. However, this degeneracy is not observed in the real trap.

The excitation is applied in a unipolar mode along the z-axis (the rotational axis), and can be considered as the sum of a dipole and a quadrupole potential. We can expect the strongest resonance to be at $\omega_z/2\pi$. Due to the geometry of excitation, resonances of the radial motion $\omega_{x,y}$ are also excited through the radial-component of the excitation potential.

Figure 2 shows the linear resonances ω_z and ω_x as well as their multiples and sub-multiples (parametric resonances [24]). The observation of these additional frequencies besides the fundamental ones is the signature of the micro/macromotion coupling due to the non-ideal shape of the trap. All the observed frequencies are reported in Figure 3. The frequency combination $\omega_z/2 + \omega_x$, which gives evidence of the coupling between the radial and axial motion component, as in [21], is also found. Indeed, for a trap of cylindrical shape, the fields and equations of ion motion depend on x, y and z [25], contrary to the case of an ideal Paul trap where the axial and radial motion are uncoupled. Moreover, the cooling laser-beam which

crosses the trap diagonally couples the different degrees of freedom.

The potential of the described device is similar to that of an ideal Paul trap only in the center area of the ring. Hence, in order to produce the same potential well depth as in the ideal Paul trap, the voltages applied to the cylindrical miniature trap have to be higher. In order to keep the definition of the parameters of stability, a and q, of the Paul-Straubel trap compatible with the "traditional" case, a correction factor $\mathcal{L}$ must be introduced in the relations (2) [8]:

$$a_z = \frac{8eU_{\mathrm{DC}}}{mr_1^2\Omega^2\mathcal{L}} \quad \text{and} \quad q_z = -\frac{4eV_{\mathrm{AC}}}{mr_1^2\Omega^2\mathcal{L}}\,. \tag{5}$$

Experimental and theoretical studies have shown that for the "standard" Paul ion trap the maximum cloud size can be found at working parameters around $q_z = 0.55$ and $a_z = -0.03$ [26–28]. Taking into account these values in the measurements of the amplitude of fluorescence as a function of the applied V_{AC} allows us to make a first estimation of the correction factor of our trap to be $\mathcal{L} = 6.8 \pm 0.5$. A more precise technique for calculating this correction factor for a given working point, consists in measuring the fundamental frequencies of the ion motion. With equation (5) it is actually possible to estimate $\mathcal{L}$ using the adiabatic approximation along the q_z-axis of the stability diagram where $U_{\mathrm{DC}} = 0$.

The correction factor $\mathcal{L}$ was evaluated from the measured values of ω_x and ω_z. In order to explain the observations mentioned above, it appears necessary to define a correction factor for each direction. Equations (1) have to be replaced by [8]

$$a_z\mathcal{L}_z = -2a_x\mathcal{L}_x \quad \text{and} \quad q_z\mathcal{L}_z = -2q_x\mathcal{L}_x. \tag{6}$$

These correction factors take into account the different causes of deviations from the ideal case. The main contribution for $\mathcal{L}$ is the loss of trapping efficiency of the cylindrical trap compared to an ideal Paul trap due to the discrepancy between the presented geometry and the quadrupolar one. In fact, the geometric defects are not identical in the radial and axial direction, the trapping efficiency is therefore modified in a different way for x and z. In our experiment, patch potential effects may build up over time mainly on the ring electrode. This would lead to a distortion in the symmetry of revolution of the confinement potential. The effect on the loss factor would then concern a possible difference between the x and y-directions. An effect of the patch potential should show a (slight) evolution in the course of time. The presented measurements have been carried out over a period of a couple of weeks without showing any modification caused by the build-up of a contact potential.

The larger the cloud is, the further away from its center are the ions and therefore the values of $\mathcal{L}_z$ and $\mathcal{L}_x$ are subject to variation. It has been observed experimentally, that for rf potentials increasing from 580 to $790V_{\mathrm{rms}}$, $\mathcal{L}_z$ decreases from 8.0 to 7.6, whereas $\mathcal{L}_x$ increases very slowly from 7.0 to 7.1. For a very high rf potential, the well depth increases and the two correction factors should become even closer since the ion cloud is concentrated in the center of the trap, where the potential shape is less sensitive to deviations from the quadrupole case.

4 Characterization of the stability diagram

Theoretical and experimental studies have shown that the stability diagram and the frequencies of motion of an ion cloud in a trap of cylindrical geometry can be calculated in a similar way to its hyperbolic counterpart with identical dimensions r_0 and z_0 [25,29]. In fact, while changing from the hyperboloidal geometry to a cylindrical one, the limits of the Mathieu stability diagram tend to smaller a, q-values while the influence of space charge shifts the diagram to higher values. In order to define the effective boundaries of the stability diagram the following experimental procedure was run. In the first step, an ion cloud ($\sim$ 500 ions) is created at an rf voltage V_{AC} with a zero potential U_{DC} applied to the endcaps. Then, a positive (or negative) potential U_{DC} is applied to the endcaps (which is equivalent to the application of $-U_{\mathrm{DC}}$ on the ring) and is slowly increased from 0 to $\pm$150 V. During this scan, the overall fluorescence of the ion cloud is recorded. The boundaries of the stability diagram are clearly illustrated by the disappearance of any fluorescence signal due to the complete loss of the ions. A new cloud must be created for each scan and this is always done at $U_{\mathrm{DC}} = 0$. These measurements have been carried out for V_{AC} varying between 500 and $1000V_{\mathrm{rms}}$.

For a clear visualisation, we need to draw the effective iso-β lines and thus to calculate β_x and β_z. Using the correction factor $\mathcal{L}_{x,z}$, equations (5) transform the measured boundaries from (U_{DC}, V_{AC}) coordinates into (a_z, q_z) coordinates (see Fig. 4). We have used the mean values of Section 3, $\mathcal{L}_z = 7.8 \pm 0.2$ and $\mathcal{L}_x = 7.05 \pm 0.05$. This is more accurate than to use an average value shared by the two directions; a common value plainly could not reflect the real behaviour of the potential. In our experiment, $U_{\mathrm{DC}} = 150$ V corresponds to $a_z = 0.14$ and $V_{\mathrm{AC}} = 1000V_{\mathrm{rms}}$ leads to $q_z = 0.66$.

The resulting measured limits of the stability diagram reproduce the form of the theoretical stability region, except for its right-hand side boundary, theoretically defined by $\beta_z = 1$ (see Fig. 4). We observed that no ion cloud could survive the crossing of this right-hand-side border. Furthermore, all attempts to create and to trap ions on the other side of this border ($1000V_{\mathrm{rms}} < V_{\mathrm{AC}} < 1400V_{\mathrm{rms}}$ and $U_{\mathrm{DC}} = 0$) failed. We thus considered this right-hand side boundary to be the real limit of the stability diagram of the trap. A similar reduction of the surface of the stability diagram compared to the ideal Paul-trap shape has been predicted by Benilan *et al.* [25]. In a theoretical study, they have found that the limits of the stability diagram of a cylindrical trap are shifted to smaller values of q_z when the dimensions z_1 and r_1 approach each other. In this case, the $\beta_z = 1$ limit crosses the q_z-axis at $q_z = 0.65$ for $r_1 = z_1$ (instead of $q_z = 0.908$ for an ideal Paul trap). Yet, a more precise analysis of the experimental stability

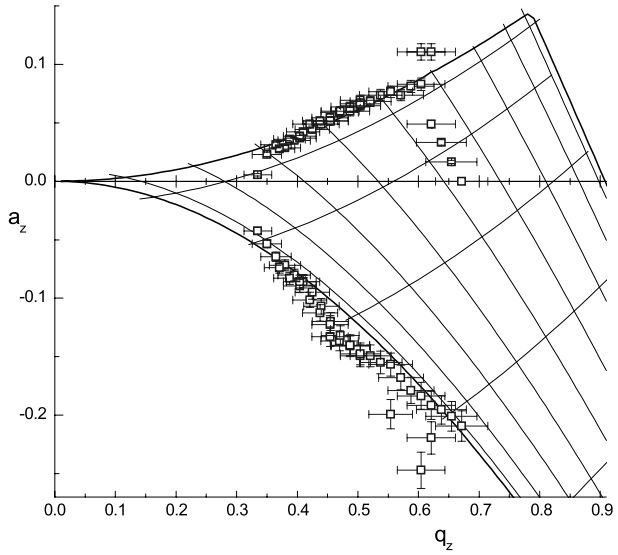

Fig. 4. Limits of the stability diagram as observed from the fluorescence of a small Ca^+-ion cloud as compared to the stability diagram of an ideal Paul trap (solid lines). The observed right-hand-side limit corresponds to a $\beta_z = 1/2$ canyon, no ion could be confined beyond this boundary.

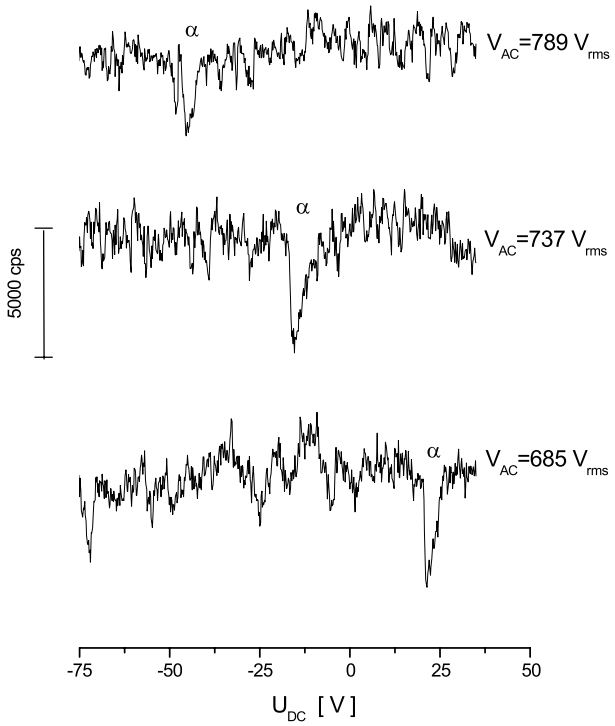

Fig. 5. Cross-section of the stability diagram for different values of $V_{\rm AC}$. The canyon α – which corresponds to $\beta_z = 1/3$ – can be tracked for various working points.

diagram taking into account the ω_z measurements shows that the observed right-hand side border actually corresponds to a $\beta_z = 1/2$ canyon. The non-linear resonances occurring along this line are so strong that no ions can stay in the trap. Moreover, on the high-q_z side of the $\beta_z = 1/2$ canyon, a multitude of very close lying canyons can exist [12,30].

Another characterization of the ion cloud consists in locating its motional resonances in a ($V_{\rm AC}$, $U_{\rm DC}$) diagram visualized by the absences in the fluorescence signal for given combinations of ($V_{\rm AC}, U_{\rm DC}$)-values. A good knowledge of the position of these canyons is very important in order to select the best trapping parameters. We record the fluorescence emitted by the cloud at fixed values of the rf potential $V_{\rm AC}$, while slowly scanning the potential $U_{\rm DC}$ from 0 to $\pm$150 V. For neighbouring $V_{\rm AC}$ values, a given non-linear resonance can be tracked in the stability diagram as shown in Figure 5. We may thus visualize a canyon in the stability diagram, characterized by a constant rational β_x or β_z value or a combination of them. The assignment of the "effective" β_x or β_z-values (using $\mathcal{L}_x$ and $\mathcal{L}_z$) gives a projection of the inner shape of the stability diagram. In Figure 6 the identified canyons with their assignments are plotted. We could isolate four rational iso-β_x and three rational iso-β_z canyons. Most of these canyons can be assigned with a precision better than 4%. The assignment of the canyons $\beta_x = 2/9$ and $\beta_x = 1/6$ can only be made to the 7%-level. In Figure 6 these canyons can also be seen to have a slightly deviated direction. Finally, the $\beta_z = 1/3$ canyon is found with a 10%-precision, in fact these resonances have been observed to be large. The assignment has also been confirmed by consideration of the inter-canyon distance. All these canyons prove the existence of couplings between the macromotion along the

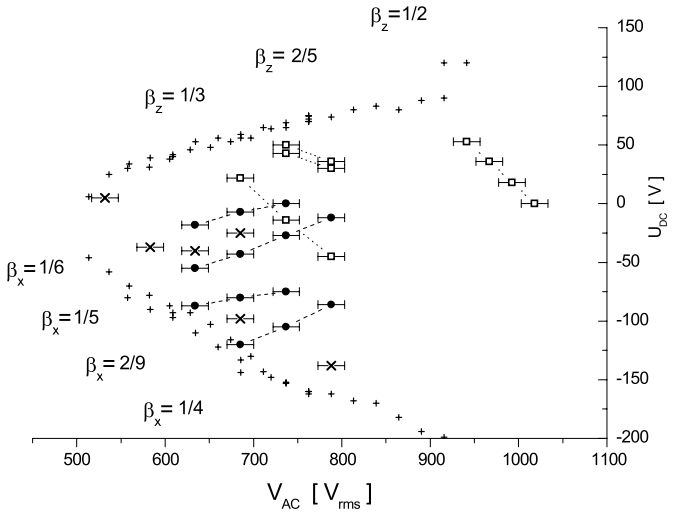

Fig. 6. "Black canyons" in a part of the stability diagram. Points of low confinement coincide with lines of constant rational β_x or β_z indicating a coupling of the macro- and the micromotion. The lines are a guide to the eye, and indicate points of identical β-value. (□) and (•) stand for iso-β_z and β_x-canyons respectively. The measured limits of the stability diagram are visualized by (+), for clarity the error bars on these values have been omitted in this graph. A few strong resonances (indicated by ×) could not be assigned with a common β-value at the 5%-level.

axial and the radial directions with the rf pulsation [12]. One of the resonances we observe ($\beta_z = 2/5$) presents a doubling of its structure. This kind of doubling could be explained by a defect of the axial symmetry of the trap. The canyons observed and assigned inside the stability region are consistent with the previous assignation of the $\beta_z = 1/2$ canyon. The present experimental stability diagram shows that, for the characterization of such a device as the miniature trap, the stability diagram boundaries alone, do not provide enough reliable information.

5 Evaluation of the effects of the radiation pressure

The possibility of measuring a shift of the motion frequencies with high precision can show evidence even for very small effects as, for example, the influence of a friction force $-\rho v$ (with ρ the damping factor, and v the velocity of the ions) on the shape of the stability diagram, as calculated by Winter and Ortjohann [31] for macroscopic particles in an air flow. These authors have shown that the stability diagram can be modified a lot by a friction force as soon as the ratio $2\rho/m\Omega$ (m the mass of the ion) reaches values close to one. Furthermore, numerical simulations concerning ions have suggested that $2\rho/m\Omega$ must become of the order of 1 to produce a non-negligible distortion of the stability diagramm [33].

The radiation pressure force has been studied in many articles for cooling of free neutral atoms as well as trapped ions. As the natural frequency width $\Gamma/2\pi$ of the transition involved in the cooling (23 MHz) is larger than the frequencies of micro- and macromotion $\Omega/2\pi$, $\omega_z/2\pi$ and $\omega_x/2\pi$ (11.6 MHz, 1.5 MHz and 0.75 MHz, resp.), the absorption and emission of photons by the trapped ions are the same as for free atoms [11]. We can then use the general expression of the radiation pressure force in a travelling wave along the direction of the laser propagation, as in [32]:

$$F = F_0 - \rho v \tag{7}$$

with the constant force

$$F_0 = \hbar k \frac{\Gamma}{2} \frac{s_0}{s_0 + 1 + \left(\frac{2\Delta}{\Gamma}\right)^2} \tag{8}$$

where k is the wave-vector of the 397 nm cooling laser, Δ the detuning between the laser frequency and the atomic transition frequency, s_0 is the saturation parameter in resonance, and the damping factor ρ is defined by:

$$\rho = -\hbar k^2 \frac{4 s_0 (\Delta/\Gamma)}{\left[s_0 + 1 + \left(\frac{2\Delta}{\Gamma}\right)^2\right]^2} \tag{9}$$

and is positive for red detuned light, as in our experiment.

The friction force $-\rho v$ may distort the ion dynamics and the stability diagram by introducing a damping term in the motion of the ion. The perturbations induced are largest when the damping coefficient ρ reaches its maximum value $\rho_{\max} = \hbar k^2/4$ for $\Delta = -\Gamma/2$ and $s_0 = 2$ [32]. The maximal damping can not be increased as it depends only on the transition wavelength. In our case the maximum value $\rho_{\max}$ that can be reached is 6×10^{-21} kg/s and then $2\rho/m\Omega$ can never be greater than 2.6×10^{-3} which is much smaller than one. In our experiment, the detuning Δ was of the order of 5Γ and s_0 varied roughly between 0.01 and 5 (corresponding to variation of the laser-cooling power between 8 μW and 900 μW). For even larger values of the detuning and of the saturation parameter, the damping coefficient tends toward zero and no friction force occurs. We checked the radiation pressure influence on the observed mechanical resonances by looking at the frequency spectra. Once the cooling transition $4S_{1/2}$–$4P_{1/2}$ is no longer saturated (for laser power values below 200 μW) we can observe that the width of the resonances increases while the cloud becomes hotter. There is no detectable shift in the ω-values. Therefore we cannot expect any significant modification of the stability diagram, whatever the laser cooling power. An influence of the friction force would be detectable in other experiments using lighter ions and lower trapping frequencies.

Furthermore, the radiation pressure force could have another effect on the dynamics of the cloud. Besides a damping component, this force also has a constant term F_0 (see Eq. (7)) which has the same effect as a constant and uniform electric field: it shifts the mean position of an ion in the rf trap along the laser beam propagation direction [34]. As the laser beam has non-zero projections on the z-axis and on the radial plane (along a direction we call X_{L}), the mean position of an ion is shifted in these two directions by the amounts

$$\Delta Z = \frac{F_{0_z}}{m\omega_z^2} \quad \text{and} \quad \Delta X_{\mathrm{L}} = \frac{F_{0_{x_{\mathrm{L}}}}}{m\omega_x^2} \tag{10}$$

where m is the mass of a calcium ion. The upper limit of the force F_0 is given by $\hbar k\Gamma/2$. This maximum value causes a translational shift of the ions of about 10 nm in both directions and will not modify here the dynamics of the cloud in the trap.

6 Conclusion

In this paper we have reported on the construction and the implementation of a miniature cylindrical ion cage. In order to work under metrologic conditions, it is imperative to characterize the trap boundaries in a precise way to be able to make a sound choice of the working parameters. The trapping characteristics were explored by confining a laser-cooled Ca^+-ion cloud and observing its properties. We infer that the measurement of the limits of the stability diagram alone do not provide sufficient information. The measurements of the motional resonances of the cloud and the pursuit of their evolution throughout the stability diagram have been corroborated by a method detecting the non-linear resonances in the trap. In particular, the actual

β_z-boundary value of 1/2 instead of 1 is a signature of the considerable inhomogeneity of the first zone of the stability diagram in the capability to confine. The correction factors, $\mathcal{L}_z$ and $\mathcal{L}_x$, are found to be different, due to the asymmetric distortion of the miniature trap geometry. In the final step, we have evaluated the order of magnitude for the influence of the radiation pressure force on the ion dynamics and on their positions in the trap. For the Ca^+ ions, these values lie below the spectral as well as the spatial limit of the detection. The present characterization of the miniature trap contributes to the catalogue of small geometries for new mass spectrometry and will enable us in the close future to choose the optimal working conditions to capture one single Ca^+ ion and to put it in the quasi zero-field area of the trap.

References

1. W. Paul, Rev. Mod. Phys. **62**, 531 (1990).
2. *Proceedings of the Fifth Symposium on Frequency Standards and Metrology*, edited by J.C. Bergquist (World Scientific Ltd, Singapore, 1996).
3. K. Enders, E. Stachowska, G. Marx, C. Zölch, U. Georg, J. Dembcczynski, G. Werth, Phys. Rev. A **56**, 265 (1997).
4. Pratical Aspects of Ion Trap Mass Spectrometry, Vols. 1–3 of *Modern Mass Spectrometry*, edited by R. March, J. Todd (CRC Press, New York, 1995).
5. W. Neuhauser, M. Hohenstatt, P.E. Toschek, H. Dehmelt, Phys. Rev. Lett. **12**, 233 (1978).
6. E. Beaty, J. Appl. Phys. **61**, 2118 (1987).
7. N. Yu, W. Nagourney, H. Dehmelt, J. Appl. Phys. **6**, 3779 (1991).
8. C. Schrama, E. Peik, W. Smith, H. Walther, Opt. Commun. **101**, 32 (1993).
9. E. Badman, R. Johnson, W. Plass, R. Cooks, Anal. Chem. **70**, 4896 (1998).
10. C.-S. O, H. Schuessler, Int. J. Mass Spectr. Ion Proc. **35**, 305 (1980).
11. D. Wineland, W. Itano, Phys. Rev. A **20**, 1521 (1979).
12. Y. Wang, J. Franzen, K. Wanczek, Int. J. Mass Spectr. Ion Phys. **124**, 125 (1993).
13. D. Eades, J. Johnson, R. Yost, J. Am. Soc. Mass Spectr. **4**, 917 (1993).
14. G. Werth, in *Frequency standards and metrology*, edited by A. de Marchi (Springer-Verlag, Berlin, Heidelberg, 1989), pp. 293, 299.
15. A. Madej, J. Bernard, in *Frequency Measurement and Control*, *Topics in Applied Physics*, edited by A. Luiten (Springer Verlag, New York, 2000).
16. M. Knoop, M. Vedel, F. Vedel, Phys. Rev. A **52**, 3763 (1995).
17. E. Biemont, C. Zeippen, Comm. At. Mol. Phys. **33**, 29 (1996), and references therein.
18. H. Straubel, Naturwissenshaften **18**, 506 (1955).
19. F. Vedel, M. Vedel, Phys. Rev. A **41**, 2348 (1990).
20. R. Alheit, C. Henning, R. Morgenstern, F. Vedel, G. Werth, Appl. Phys. B **61**, 277 (1995).
21. M. Vedel, J. Rocher, M. Knoop, F. Vedel, Appl. Phys. B **66**, 191 (1998).
22. R. March, R. Hughes, in Quadrupole Storage Mass Spectrometry, Vol. 102 of *Chemical analysis*, edited by J. Winefordner (John Wiley and Sons, New York, 1989).
23. H. Dehmelt, Adv. At. Mol. Phys. **3**, 53 (1967).
24. L. Landau, E. Lifschitz, *Mécanique* (Mir, Moscou, 1966), Vol. 102.
25. M.-N. Benilan, C. Audoin, Int. J. Mass Spectr. Ion Proc. **11**, 421 (1973).
26. M. Baril, A. Septier, Rev. Phys. Appl. **9**, 525 (1974).
27. R. Ifflaender, G. Werth, Metrologia **13**, 167 (1977).
28. M. Vedel, J. André, S. Chaillat-Negrel, F. Vedel, J. Phys. France **42**, 541 (1981).
29. R. Mather, R. Waldren, J. Todd, R. March, Int. J. Mass Spectr. Ion Phys. **33**, 201 (1980).
30. R. Alheit, S. Kleineidam, F. Vedel, M. Vedel, G. Werth, Int. J. Mass Spectr. Ion Proc. **154**, 155 (1996).
31. H. Winter, H. Ortjohann, Am. J. Phys. **59**, 807 (1991).
32. H. Metcalf, P. van der Straten, *Laser cooling and trapping* (Springer Verlag, New York, 1999).
33. R. Blümel, Phys. Rev. A **51**, 620 (1995).
34. D. Berkeland, J. Miller, J. Bergquist, W. Itano, D. Wineland, J. Appl. Phys. **83**, 5025 (1998).